A high-efficient antibacterial and biocompatible polyurethane film with Ag@rGO nanostructures prepared by microwave-assisted method: Physicochemical and dermal wound healing evaluation

Abbas Mohammadi [a,*], Zahra Ghorbanian Kerdabadi [b], Seyed Ahmad Ayati Najafabadi [c], Alireza Pourali [b], Fereshteh Nejaddehbashi [d], Nastaran Azarbarz [d], Kaveh Hatami Kahkesh [e], Mehrnoosh Ebrahimibagha [f]

[a] *Department of Chemistry, University of Isfahan, Isfahan 81746-73441, I.R. Iran*
[b] *School of Chemistry, Damghan University, 36716-41167 Damghan, Iran*
[c] *Department of Biomaterials, Tissue Engineering and Nanotechnology, School of Advanced Technologies in Medicine, Isfahan University of Medical Sciences, Isfahan, Iran*
[d] *Cellular and Molecular Research Center, Medical Basic Sciences Institute, Ahvaz Jundishapur University of Medical Sciences, Ahvaz, Iran*
[e] *Department of Basic Medical Science, Faculty of Veterinary Medicine, Shahrekord University, Shahrekord, Iran*
[f] *Tissue Engineering and Regenerative Medicine Institute, Central Tehran Branch, Islamic Azad University, Tehran, Iran*

ARTICLE INFO

ABSTRACT

Wound infections are a significant issue that can hinder the wound healing process. One way to address this problem is by enhancing the antibacterial activity of wound dressings. Accordingly, this work focuses on developing a castor-oil-based antibacterial polyurethane nanocomposite film impregnated with silver nanoparticles (AgNPs) decorated on the surface of reduced graphene oxide (rGO) nanostructures (Ag@rGO). To this aim, rGOs act as a platform to stabilize AgNPs and improve their bioavailability and dispersion quality within the PU film. The microwave-assisted synthesis of Ag@rGO nanohybrids was proved by FTIR, XRD, TGA, FE-SEM, EDS, and TEM analyses. Compared to PU/GO, the effect of Ag@rGO nanohybrids on thermo-mechanical features, morphology, antibacterial activity, cytocompatibility, and in vivo wound healing was assessed. SEM photomicrographs revealed the enhanced dispersion of Ag@rGO nanohybrids compared to GO nanosheets. Besides, according to XRD results, PU/Ag@rGO nanocomposite film demonstrated higher microphase mixing, which could be due to the finely dispersed Ag@rGO nanostructures interrupting the hydrogen bonding interactions in the hard segments. Moreover, PU/Ag@rGO nanocomposite showed excellent antibacterial behavior with completely killing *E. coli* and *S. aureus* bacteria. In vitro and in vivo wound healing studies displayed PU/Ag@rGO film effectively stimulated fibroblast cells proliferation, migration and re-epithelialization. However, the prepared antibacterial PU/Ag@rGO nanocomposite film has the potential to be used as a biomaterial for dermal wound healing applications.

* Corresponding author
   E-mail addresses: a.mohammadi@sci.ui.ac.ir, abbaspolymer66@gmail.com (A. Mohammadi).

1. Introduction

The skin as biggest organ covers the human body and made up of the epidermis, dermis, and hypodermis [1]. As a vital barrier, the skin can play a big part in protecting the human body against environmental agents [2]. However, if this defensive barrier is defected through wound formation, the skin's function and normal anatomical structure can be disrupted. This disruption can lead to the easy penetration of microorganisms like bacteria and fungi, causing the formation of infection in the wound environment [3,4]. In the case of serious wounds, due to the infection, the skin cannot take part in the self-healing process. This problem can complicate the situation, delaying the wound-healing process or leading to the patient's death [4,5]. As a result, it is essential to protect the damaged skin of a wound from infection and provide support to heal the wound properly and quickly by fabricating modern wound dressings. These novel biomaterials can not only cover the wound bed but also prevent the invasion of pathogens and infection [6,7]. Recently, the utilization of renewable materials with potential biomedical properties is considered as a novel strategy to fabricate wound dressings. This aims to accelerate wound healing with minimal side effects, including scar tissue formation and cell toxicity [8–10]. These renewable materials have been commonly investigated to form scaffolds, films, and hydrogels as bioactive wound covers [11]. However, the latest advances in designing skin replacements show that researchers focus on using renewable components for designing and developing biomedical-grade polymers.

Polyurethanes (PUs) have been considered an excellent candidate for preparing modern dressings. This is due to their great diversity of construction units, including diisocyanates, polyols and chain extenders. These environmentally-friendly PUs have widely favorable chemical and physical properties such as good oxygen and water vapor permeability and barrier properties, variable mechanical properties, and nontoxicity [12–14].

A tremendous effort has been made to use vegetable oils to synthesize non-toxic and biocompatible, environmentally friendly and cheaper PUs [15,16]. Among vegetable oils, castor oil (CO) can be used as green polyol to manufacture bio-based PUs [17]. In addition, CO has demonstrated potent curative effects on the treatment of wounds due to its excellent anti-inflammatory properties [18]. Moreover, CO base polyurethanes can be a desired polymeric matrix to produce highly efficient wound dressings by incorporating different nanoparticles, drugs and biological compounds.

Researchers have been focusing on developing effective antimicrobial PU wound dressings using various inorganic antibacterial materials such as metal cations (e.g., zinc, copper, and silver) or their complexes [19], nanoparticles (e.g., Ag, Au, ZnO, and TiO_2) [20–22]. These antibacterial active substances may face practical limitations such as poor solubility, low dispersion quality, low stability, undesired bioavailability and no long-term antibacterial effect. Additionally, rapid release and toxicity towards cells can also be of concern [23–25]. It's important to consider these limitations when developing polyurethane wound dressings based on inorganic antibacterial agents. These shortcomings may be overcome by hybridization strategies which can stabilize them and improve their dispersion quality. It's also promising that this approach has led to prolonged antibacterial efficacy and improved cell compatibility with lower concentrations of inorganic antibacterial materials [26,27].

Among antibacterial nanoparticles, AgNPs have been proposed as a promising agent against Gram-positive and Gram-negative bacteria, which have been shown to be less prone to antibiotic resistance compared to traditional antibiotics [28,29]. It is thought that the potential antibacterial behavior of AgNPs is related to the interaction of released Ag^+ ions from NPs with the cell wall, enzymes, proteins and nucleic acid of bacteria [30–34]. Unfortunately, the antibacterial applications of AgNPs can be affected by two main limitations, including a strong tendency to aggregate and also cell toxicity [35,36]. There are various methods used to produce silver nanoparticles (AgNPs), including chemical, biological, and physical methods. One common method involves reducing silver ions (Ag^+) from a silver salt solution using reducing agents [37].

Various reducing agents have been used in the synthesis of silver nanoparticles (AgNPs), including hydrazine [38], sodium borohydride ($NaBH_4$) [39], polyethylene glycol (PEG) [40]. The reducing agent type has a drastic effect on various factors such as size and shape of the nanoparticles. The use of environmentally friendly reducing agents such as chitosan [41] and glucose [42] is becoming increasingly popular due to their biocompatibility and low toxicity. Some eco-friendly reductants like sodium citrate are milder and slower in reducing silver ions compared to conventional reducing agents like hydrazine or sodium borohydride. This can result in a longer reduction process, requiring more time for the synthesis of silver nanoparticles [43,44]. Various strategies, including adjusting the reaction conditions such as temperature and pH, increasing the concentration of the reducing agent and adding catalysts or additives can be used to increase the reduction rate of silver ions [45,46]. Moreover, microwave-assisted synthesis is a high-performance tool for the uniform, high yield and fast preparation of silver nanoparticles. This is because microwave irradiation can provide localized heating, leading to enhanced electron transfer from the reducing agent to the silver ions, thereby promoting faster and more efficient reduction rates [47,48].

Stabilizing agents play a crucial role in the preparation of AgNPs. These agents are used to prevent agglomeration of the nanoparticles and to control their nanostructure [49]. Graphene oxide (GO) nanosheets have been studied as a support for stabilizing, preventing agglomeration and uniform dispersing silver nanoparticles (AgNPs) in polymeric matrices. The use of GO as a support offers several advantages, including high surface area, good biocompatibility, and the ability to functionalize the surface with various chemical groups. This can also improve the stabilization and bioavailability of AgNPs and thereby enhance their antibacterial properties. The presence of oxygen-containing functional groups, such as hydroxyl, epoxy and carboxyl groups on the surface and edges of graphene oxide (GO) nanosheets provides anchoring sites for the attachment of silver nanoparticles (AgNPs). In fact, these functional groups can serve as binding sites for metal ions, facilitating the reduction and deposition of AgNPs onto the GO surface [50, 51].

In this work, a potent antibacterial wound dressing film was developed based on castor oil-based polyurethane nanocomposite containing Ag@rGO hybrid nanostructure. To this aim, firstly, Ag@rGO nanostructure was prepared via microwave-assisted method

using sodium citrate as a cost-effective and environmentally friendly reducing agent for both GO nanosheets and silver ions. It is worth noting that graphene oxide, as a stabilizing agent through its anchoring sites, helps to prevent the agglomeration of AgNPs, while also promoting uniform dispersion and high bioavailability of AgNPs in the PU matrix. To the best of our knowledge, a PU/Ag@rGO nanocomposite film with such high bactericidal activity against both gram-negative *E. coli* and gram-positive *S. aureus* bacteria, along with potent dermal wound healing efficacy, has not been fabricated thus far.

2. Experimental

2.1. Materials

To synthesize treated and untreated GO nanostructures, the main ingredients: graphite flakes (95 %) were purchased from DaeJung Chemicals&Metals, South Korea; potassium permanganate ($KMnO_4$), Sulfuric acid (H_2SO_4, 98 wt%), hydrogen peroxide (H_2O_2, 30 wt %), orthophosphoric acid (85 wt%), silver nitrate ($AgNO_3$, 99 %) and sodium citrate were obtained from Merck, Germany. To fabricate PU films, isophorone diisocyanate (IPDI, Merck), diethylene glycol (DEG, Aldrich) and castor oil (CO, Aldrich) were all analytical agents grades without any further purification.

2.2. Synthesis of GO and Ag@rGO nanostructures

GO was prepared based on our previous work [3]. Then, AgNPs were decorated onto GO nanosheets in a typical *in-situ* reduction procedure using a reducing reagent under microwave irradiation. First, the synthesized GO flakes (0.5 g) were dissolved in distilled water (100 mL), stirred for 30 min and then ultrasonically dispersed for 1 h at ambient temperature. After that, the prepared dispersion was mixed with $AgNO_3$ (0.25 g) and sodium citrate (1.0 g) as eco-friendly reducing agent while stirring for 30 min. Then the mixture was sonicated for 1 h. The reduction process was completed under microwave irradiation (LG, NeoChef MC65BR, Frequency:2.45 GHz, Power input:200 W) for 30 min. Finally, the formed Ag@rGO hybrid nanostructures were separated by a high-speed centrifugation and washed with distilled water and methanol three times and then dried at vacuum oven. The *in-situ* synthesis scheme of Ag@rGO nanohybrids is shown in Fig. 1A.

2.3. Synthesis of blank PU, PU/GO and PU/Ag@rGO nanocomposite films

PU films were made using the pre-polymerization process with the formula presented in Table 1. For the synthesis of PU/GO and PU/Ag@rGO samples, the required amount of GO and Ag@rGO nanostructures were separately mixed with CO (5.0 g) in a four-necked reactor under gentle stirring for 24 h at room temperature. Next, NCO-terminated PU prepolymers were prepared by adding IPDI (3.36 g) under mechanical stirring for 3 h at 80 °C. Then, DEG (0.76 g) was charged as a chain extender, and the mixture was stirred for 5 min. A Blank PU sample containing no nanoparticles was synthesized similarly as above. Finally, the resulting mixture was poured into
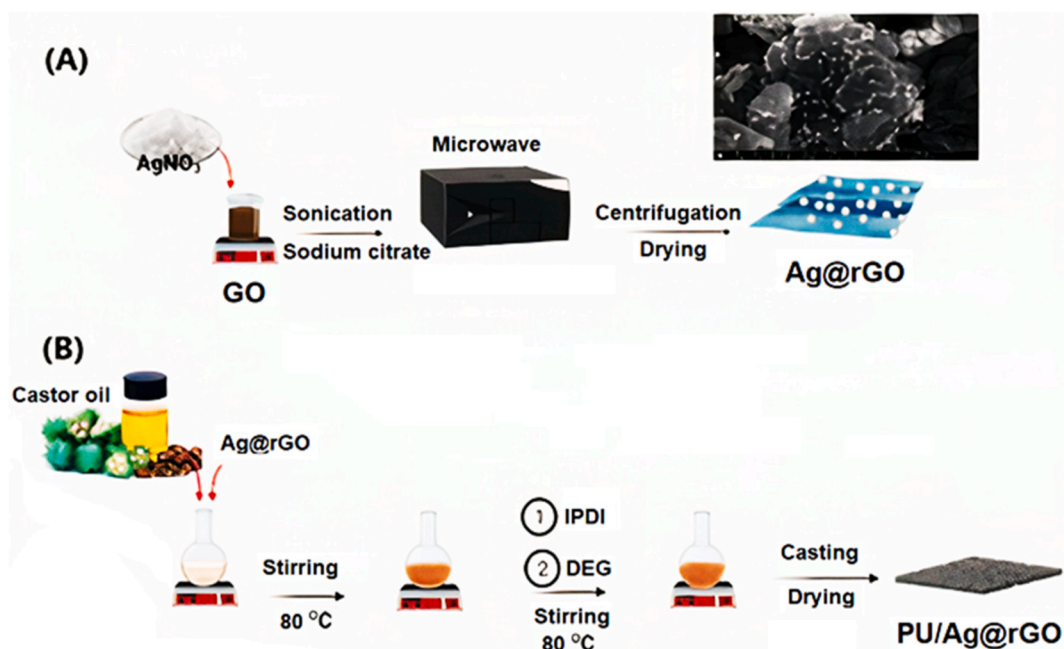

Fig. 1. The schematic synthesis of Ag@rGO nanohybrids (A) and PU/Ag@rGO nanocomposite film (B).

Table 1
The codes and formulations of Blank PU and PU nanocomposite films.

Sample	Block ratio (CO:IPDI:DEG)	Nanosheets type	Content (wt %)
Blank PU	**1:2.1:1**	–	–
PU/GO	**1:2.1:1**	**GO**	**1.0**
PU/Ag@rGO	**1:2.1:1**	**Ag@rGO**	**1.0**

a preheated Teflon mold and cured at 80 °C for 24 h. The scheme of the preparation of PU films is presented in Fig. 1B.

2.4. Measurements

FTIR and FTIR-ATR spectra were collected using a JACSO-6300 spectrophotometer. XRD analysis was performed on a Bruker D8 Advance diffractometer equipped with Cu-Kα radiation source. TGA measurements were carried out by a TGA 8000 instrument (PerkinElmer). Dynamic mechanical thermal analysis (DMTA) was provided by a DMTA-TRITON analyzer (Model Tritic 2000 DMA) to evaluate the viscoelastic properties of the prepared films in tension mode at a heating rate of 5 °C/min and frequency of 1 Hz over temperatures ranging from −50 to 100 °C. The microscopic morphology and Energy Dispersive X-ray (EDS) patterns of nanoparticles were characterized by a Dual Beam FIB/SEM microscope Helios Nano-Lab 600i (ThermoFisher Scientific, Hillsboro, OR, USA). SEM, SEM-mapping images and EDS patterns of the prepared films were provided by a scanning electron microscope (TESCAN, MIRA III, Czech Republic). Transmission electron microscopy (TEM) characterization was performed with a Zeiss Libra 120 Plus microscope operating at 120 keV, equipped with a bottom mounted 12 bit 2k x 2k CCD (TRS), and a Bruker XFlash 6T-60 SDD detector for EDS analysis.

The antibacterial performance of the obtained films towards both Gram-positive *Staphylococcus aureus* bacteria (ATCC 33591) and Gram-negative *Escherichia coli* bacteria (ATCC 35218) were investigated by a dynamic shaking flask test (according to ASTM E2149-13a standard). Briefly, bacterial suspensions from *E. coli* and *S. aureus* at concentration of 1×10^3 colony (CFU/mL) in BHI broth were prepared. Then, the films (1 cm diameter) and 250 μL of cell suspended bacteria were incubated in a Falcon tube at 37 °C for 24 h while shaking at 100 rpm. After incubation, the tube suspensions were diluted serially in BHI broth. 1 mL of the obtained bacterial suspensions (1×10^5 CFU/mL) was spread onto agar plates separately and incubated under the same condition. Finally, viable bacteria colonies were counted. Each test was repeated in triplicate.

The in vitro wound-scratch assay was performed to test cell proliferation, migration and wound closure. To achieve this aim, L929 cells were cultured with a cell density of about 5×10^4 cells/mL in 6-well plates to have a confluent cell monolayer. Then, a linear scratch "wound" was made in the middle of the cultured cell monolayer by a sterile pipette tip (1000-μL). Following this, the plates were rinsed twice with PBS to eliminate cellular debris. After adding fresh media, the prepared films (1×1 cm) were put on the created gaps. One well containing the cell suspension only without any film was served as a control. Cell proliferation and migration were monitored, and their images were taken using a Nikon Inverted Fluorescent Microscope at each incubated time-point: 0, 24, and 48 h. The images of cell-free area were used to calculate the wound area using the image J public domain software. Alternatively, the cell migration rate can also be assessed as the percent reduction of the wound closure over time:

$$\text{Wound Closure } \% = \left(\frac{A_0 - A_t}{A_0} \right) \times 100 \tag{1}$$

A_0 = the wound area calculated immediately after creating the scratch.
A_t = the wound area calculated 48 h after creating the scratch.

Normally, the wound closure percentage will rise as the migration rate of cells into the linearly scratch area at the mentioned time intervals.

Cell morphology on the films' surface was also observed by the SEM images taken using a LEO 1455VP scanning electron microscope (Zeiss, Germany) after 4-day incubation. Prior to gold coating for SEM, the cells on the films were fixed with 2.5 % glutaraldehyde in PBS at 4 °C for 4 h. Consequently, the cells-film were dehydrated in a graded ethanol/water series (50, 70, 80, 90, 100 % v/v) for 10 min each step and then dried at 25 °C overnight.

The in vivo wound healing efficiency of highly cytocompatible and antibacterial PU/Ag@rGO film in comparison to Blank PU, PU/GO films, and cotton gauze as a negative control was evaluated using a male rat. Ethical approval (ethics code NO: IR.AJUMS.ABHC.REC.1400.077) was taken from the Research Ethics Committee of Ahvaz Jundishapur University of Medical Sciences, Ahvaz, Iran. Male Sprague-Dawley rats, weighing 200–250 g, provided from Ahvaz Jundishapur University's Animal House were assigned to four groups and each group consists of three animals. Group 1: control, group 2: Blank PU, group 3: PU/GO and group 4: PU/Ag@rGO. Before wounding, the hair on the dorsal interscapular region of the animals was shaved and cleaned with ethanol (70 %). Afterward, the rats were anesthetized by intraperitoneal injection of ketamine (40 mg/kg) and xylazine (5 mg/kg). Circular full-thickness wounds (1 cm in diameter) were made on the upper back of each animal (scapular site (C_3-T_5) area), using a surgical blade. The wounds were covered with wound dressings and gauze and fixed by surgical sutures or an elastic adhesive bandage. Animals were sacrificed by CO_2 inhalation after the 7th and 12th days of the healing process. At each time-point, the pictures of the wound areas were taken and the percentage of wound healing was measured using Image J public domain software by determining the wound surface compared to the wound without dressing. In addition, histopathological tissue assessment of biopsy samples from the wound sites on days 7 and 14 was done. Excised healed skins were fixed in formalin, dehydrated, embedded in paraffin wax, and stained with hematoxylin-eosin (H&E)

to evaluate collagen fiber density and re-epithelization. The images of paraffin-embedded tissue slices were taken by a light microscope (Olympus BX 51) equipped with an Olympus DP72 camera.

3. Results and discussion

3.1. Characterization of nanostructures

The decoration of AgNPs on GO nanosheets was examined by FTIR, XRD, TGA, FE-SEM, EDS and TEM analyses.

3.1.1. FTIR analysis

The FTIR spectra of GO and Ag@rGO nanostructures are shown in Fig. 2A. The FTIR spectrum of GO nanosheets displays that the band at 3403 cm^{-1} is related to the stretching vibrations –OH groups. The absorption band at 1720 cm^{-1} is attributed to the C=O carbonyl stretching of –COOH groups on the edge of nanosheets. The skeletal ring structure of GO (C=C) show a peak at 1623 cm^{-1} [25,52]. Also, there are peaks at 1286, 1176 and 1069 cm^{-1} assigning to C–OH bending vibrations, C–O–C, and epoxy groups stretching vibrations, respectively [53]. Regarding the Ag@rGO nanohybrids, as seen from the spectrum, due to the reduction process done by sodium citrate under microwave treatment, the absorption bands intensity corresponding to the oxygen containing functional groups were considerably decreased or disappeared [52,53].

3.1.2. XRD analysis

The XRD analysis (Fig. 2B) was used to confirm decoration of AgNPs onto the GO nanosheets. The interlayer distances of treated and untreated of GO were calculated by using the Bragg's law (nλ = 2d sin θ; λ = 1.5406 Å). Regarding GO pattern, there is a characteristic peak at 2θ = 11.55° corresponding to (001) plane with an interlayer space of 7.65 Å. The XRD pattern of Ag@rGO nanostructures can confirm the structural changes compared to GO after reduction process. Compared to GO, the X-ray pattern of Ag@rGO has low-intense peaks at 2θ = 11.55° due to depletion of some oxygen-functional groups [54]. Moreover, the XRD pattern of Ag@rGO nanohybrids showed four sharp peaks at 38.2°, 44.5°, 64.6° and 77.6° attributed to (111), (200), (220) and (311) planes (JCPDS No. 04–0783), respectively. These major diffraction peaks belong to the cubic-crystal structure of AgNPs [55]. Therefore, it can be concluded that during the reduction process in the presence of sodium citrate and microwave condition, AgNPs were formed successfully.
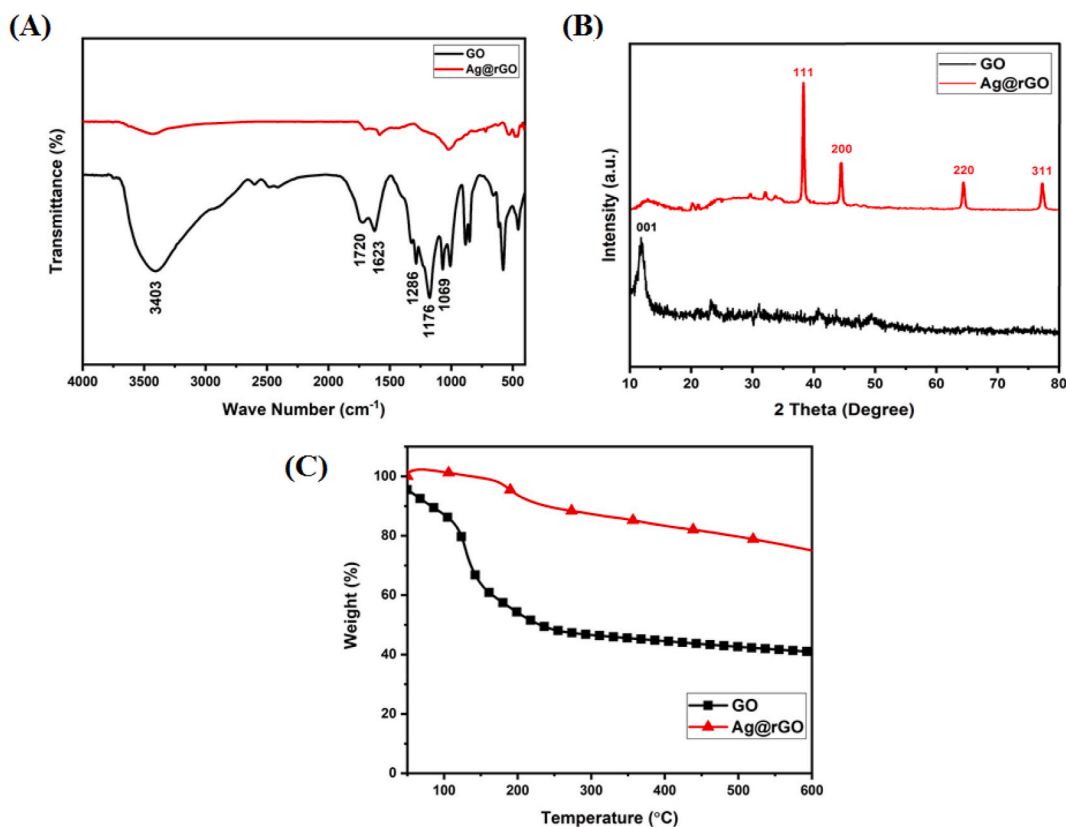

Fig. 2. FTIR spectra (A), XRD diffractograms (B) and TGA thermograms (C) of the prepared nanoparticles.

3.1.3. TGA analysis

TGA analysis was carried out to test the thermal stability and degradation behavior of GO and Ag@rGO nanostructures. TGA measurements were done under a nitrogen atmosphere in the temperature range of 50–600 °C (Fig. 2C). TGA thermogram of GO nanosheets shows three stages of thermal decomposition. Firstly, a weight loss of around 16.0 % within 50–115 °C occurred as a result of evaporation of absorbed water from GO. The second mass reduction (~36.1 %) takes place rapidly by rising temperature up to 250 °C due to the pyrolysis of unstable oxygen containing functional groups like –OH and –COOH [56,57]. In the last stage, GO lost its weight on a gentle slope from 250 to 600 °C because of the decomposition of carbon skeleton [56,58]. The thermal stability of Ag@rGO hybrids was significantly improved in comparison to the GO sample. The Ag@rGO sample showed a weight loss of only 24.9 % up to 600 °C. The reduction of GO to rGO nanosheets leads to a decrease in thermal defects at high temperatures, likely due to the reduction in the concentration of oxygen groups present in the rGO sample [57].

3.1.4. FE-SEM analysis

FE-SEM was used to observe the morphological structure of GO and Ag@rGO samples (Fig. 3). It was observed that both samples exhibit a layer-by-layer and wrinkled structure, which is consistent with the literature [59]. Based on the FE-SEM image, it can be concluded that the Ag@rGO nanocomposite was successfully formed, with AgNPs of a mean size of 24.1 nm being deposited onto the surface of rGO nanosheets. It can be noted that, the hydroxyl, carbonyl, and epoxy groups present on GO can potentially serve as coordination sites that can interact with Ag^+ ions during the reduction process, resulting in the formation of well-dispersed and less agglomerated Ag NPs on rGO layers [50,51].

3.1.5. TEM and EDS analysis

TEM micrographs were used to examine the microstructures of the GO and Ag@rGO samples, which are shown in Fig. 4A. The GO image displayed ultra-thin flakes with wrinkles, while the Ag@rGO sample image showed uniform dispersion of AgNPs throughout the rGO surfaces, with particle sizes lower than 50 nm. These findings are consistent with the results obtained from FE-SEM analysis. Furthermore, the EDS spectrum of the Ag@rGO sample exhibited signals relating to C, O, and Ag atoms, which confirms the successful formation of this nanostructure [60].

3.2. Characterization of blank and PU nanocomposite films

3.2.1. ATR-FTIR analysis

Fig. 5A shows the ATR-FTIR spectra of Blank PU, PU/GO, and PU/Ag@rGO samples. It is evident that all the samples exhibit the
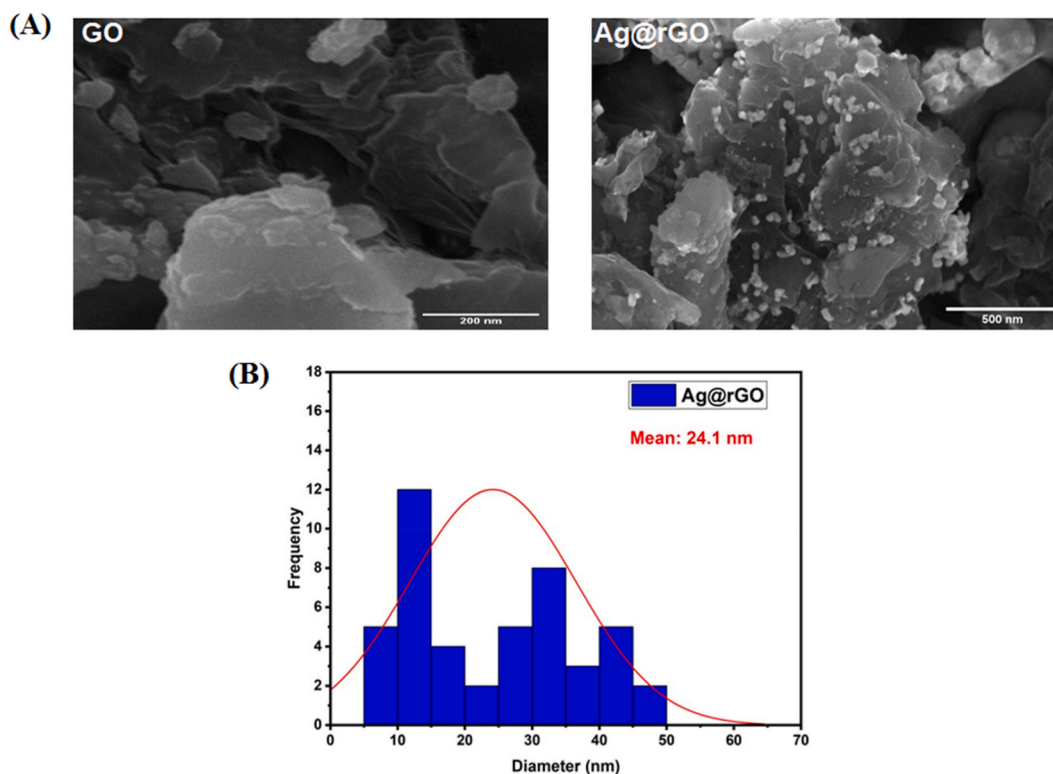

Fig. 3. FE-SEM images (A) and size distribution histogram of AgNPs formed on the rGO surface(B).
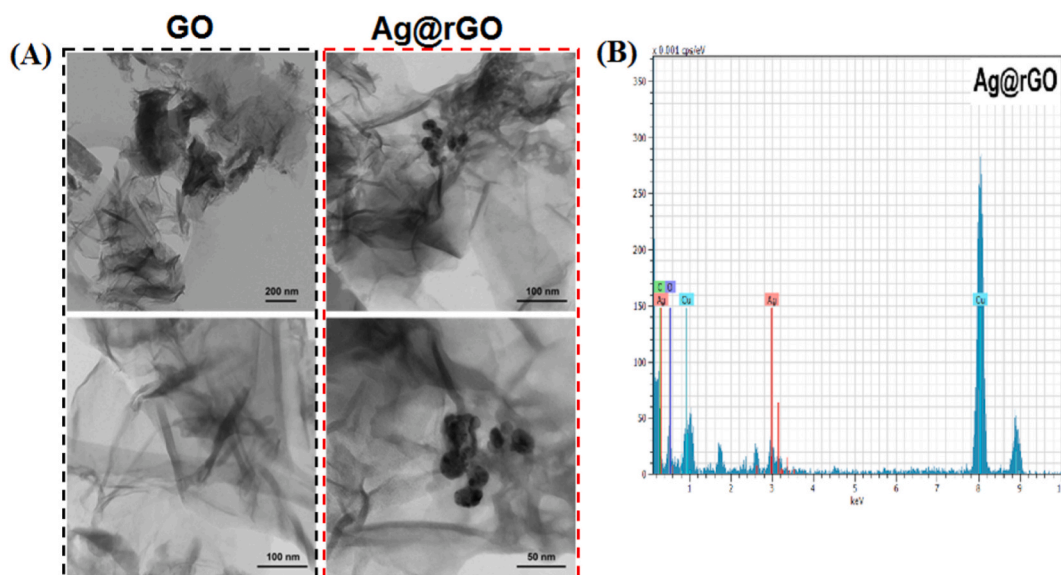
Fig. 4. TEM images (A) of GO and Ag@rGO nanostructures and EDS result of Ag@rGO nanosheets(B).
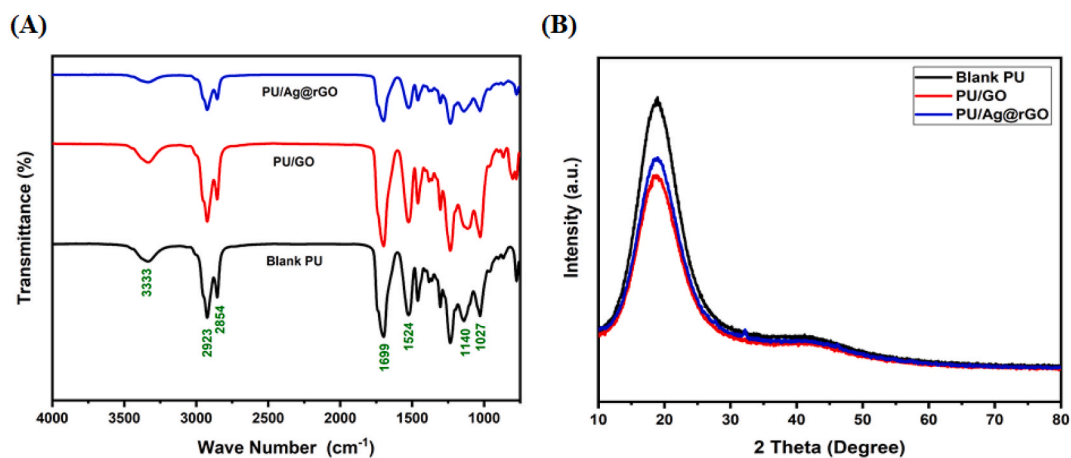

Fig. 5. ATR-FTIR spectra (A) and XRD diffractograms (B) of the fabricated PU films.

same absorption bands, confirming the formation of the PU structure without any residual isocyanate groups. The Blank PU showed an absorption peak at 3333 cm^{-1} (N–H stretching), two peaks at 2923 and 2854 cm^{-1} (C–H stretching), stretching vibration of carbonyl groups of castor oil at 1740 cm^{-1}, band at 1699 cm^{-1} (urethane carbonyl group stretching), the band at 1524 cm^{-1} (urethane N–H bending), and bands at 1140 and 1027 cm^{-1} (symmetric and asymmetric C–O stretching, respectively) [9,61,62]. For PU/GO and PU/Ag@rGO film, no significant changes were observed compared to that of Blank PU due to low introduction of GO and rGO nanostructures. Moreover, the complete disappearance of the free isocyanate peak at 2270 cm^{-1} indicates that the prepared films are non-toxic and have potential for use in biomedical applications.

3.2.2. XRD analysis

X-ray diffraction (XRD) scans were recorded to make an evaluation of the relationship between GO and Ag@rGO impregnation and the crystalline behavior of the synthesized PU films, as represented in Fig. 5B. It is accepted that the crystallization behavior of PUs mainly depends on the micro-phase separation of both hard and soft blocks. On the basis of XRD analysis, the PU sample and its nanocomposites showed a characteristic peak at 2θ = 18.8° related to soft domains, with different intensities [63]. Accordingly, the peak intensity decreased after incorporating GO and Ag@rGO nanofillers into the matrix, leading to a reduction in the degree of microphase separation. It is proposed that the GO and Ag@rGO nanostructures with hydrophilic properties disrupt the hydrogen bonding interactions within the hard domains, resulting in low phase separation and crystallinity [64,65].

3.2.3. DMTA analysis

Dynamic mechanical thermal analysis (DMTA) is an applicable technique to evaluate thermo-mechanical properties of the PU films with introduction of GO and Ag@rGO nanostructures. The logarithm of storage modulus (log E′) and loss tangent (tan δ) curves and related data are presented in Fig. 6. Based on the log E′ and tan δ plots, only one thermal transition was detected for all samples, which can be attributed to the glass transition temperature of the PU hard segments ($T_{g,HS}$). It was observed that the log E′ value decreased, especially at room temperature, for the PU/GO and PU/Ag@rGO samples compared to the Blank PU sample. Additionally, the Tg values of the PU/GO and PU/Ag@rGO samples decreased from 35.1 °C for the Blank PU to 32.5 and 30.9 °C, respectively. These findings suggest that the increase in chain movements may have arisen from the interaction of the GO and Ag@rGO nanofillers with the hard segments, which disrupts the hydrogen bonding, as mentioned earlier in the XRD section.

3.2.4. SEM analysis

The cross-sectional SEM photomicrographs of the prepared films are given in Fig. 7. Compared to the PU/GO sample, it appears that Ag@rGO exhibits improved dispersibility within the PU/Ag@rGO matrix. This is likely due to the lower concentration of polar groups, such as epoxy rings, hydroxyl, and carboxyl groups, on the surface of rGO nanosheets in Ag@rGO. As a result, Ag@rGO is able to interact more effectively with the hydrophobic soft segment (castor oil) in the PU matrix. Furthermore, it is apparent that in the PU/Ag@rGO nanocomposite, the Ag nanoparticles (AgNPs) are successfully attached to the well-exfoliated rGO surface. This leads to a highly uniform distribution of AgNPs within the PU matrix, which enhances the bactericidal properties of the nanocomposite [66].

3.2.5. Antibacterial assessment

Since bacterial infection is a major threat to wound healing, there is a need to evaluate the antibacterial properties of designed nanocomposite films before wound healing applications. For this purpose, the shake flask method was used to determine the antibacterial activity of nanocomposites against Gram-negative *E. coli* and Gram-positive *S. aureus* after 24 h of incubation. (Fig. 8). The Blank PU was considered as a negative control. It was observed that the PU/GO nanocomposite exhibited significant antibacterial properties upon contact with *S. aureus* bacteria. However, no antibacterial activity against *E. coli* was detected. The observed antibacterial capability of the PU/GO nanocomposite against *S. aureus* bacteria can be attributed to the sharp edges and reactive oxygen groups present in the GO, which are believed to cause damage to the bacterial cell walls. In fact, the sharpened edges of GO act like blades that can diffuse into and cut the cell membrane, leading to the efflux of phospholipids. Additionally, they can facilitate a finer charge transfer with the cell walls, ultimately leading to cell death [67].

As a promising and important accomplishment, the PU/Ag@rGO sample exhibited excellent bacteria-killing activity by killing 100 % of bacteria cells against both *E. coli* and *S. aureus*. This might be attributed to the synergistic effect of AgNPs and rGO nanosheets. Besides, rGO nanosheets with high surface areas supported and dispersed the impregnated AgNPs finely and uniformly within the PUmatrix, which made AgNPs more accessible to bacterial cells. This excellent antimicrobial performance of PU/Ag@rGO nanocomposite film can be considered as a potential wound dressing with powerful bacterial killing activity on the wound bed.

3.2.6. In vitro wound-scratch assay

To examine the biocompatibility and wound-healing capability of the prepared films, the in vitro wound-scratch assay was employed. To this aim, the migratory and proliferative effects of the impregnated nanoparticles on L929 fibroblast cells and wound closure were observed. The coverage rate of the scratched area was observed up to 48 h after creating the wound scratch. Fig. 9A represents the degree of proliferation and migration of fibroblast cells in response to the prepared films. Furthermore, Fig. 9B shows the quantitative results related to the wound area and wound closure percentage values after 48 h. PU/Ag@rGO film revealed the significant cell migration into the wound area and had excellent wound healing properties compared to the Blank PU and PU/GO films. According to Fig. 9C, after 48 h, the mean percentage of wound closure for the PU/Ag@rGO sample (72.1 %) was significantly higher
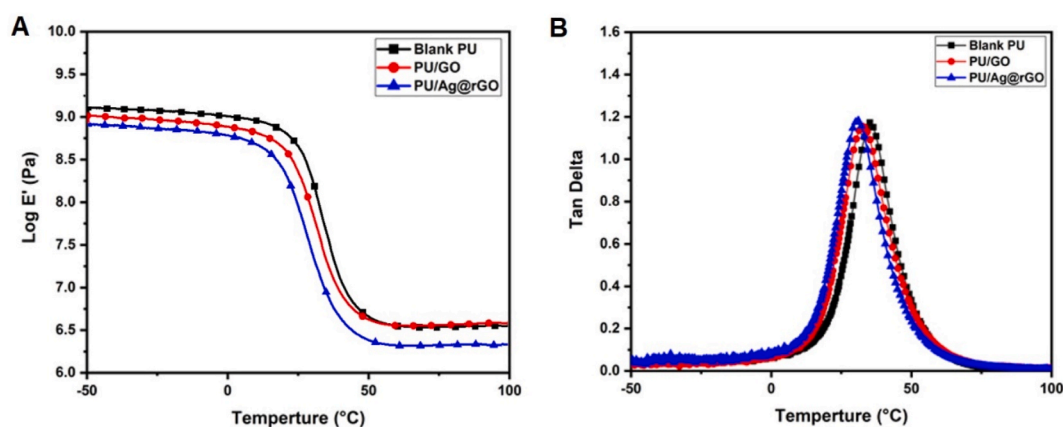

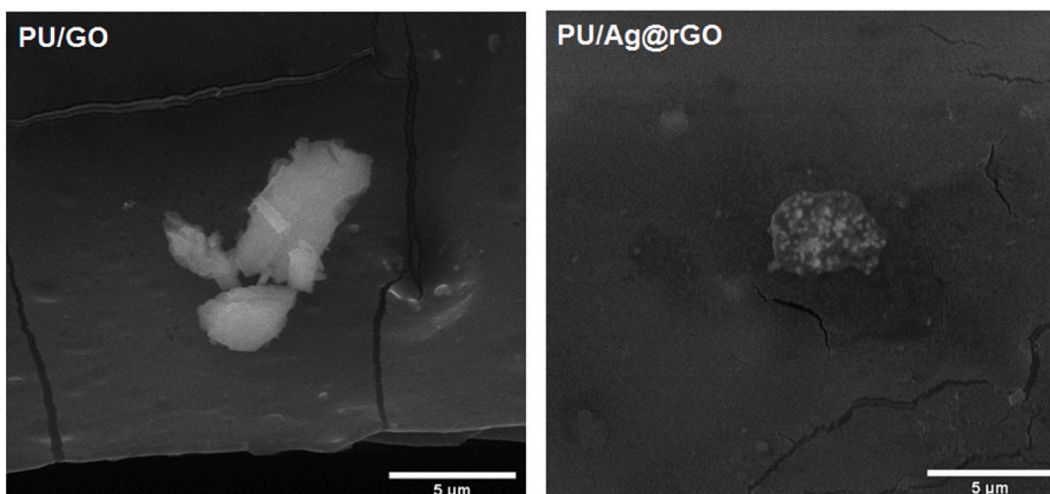**Fig. 6.** Logarithm of storage modulus (A) and tan δ (B) curves of the prepared PU films.

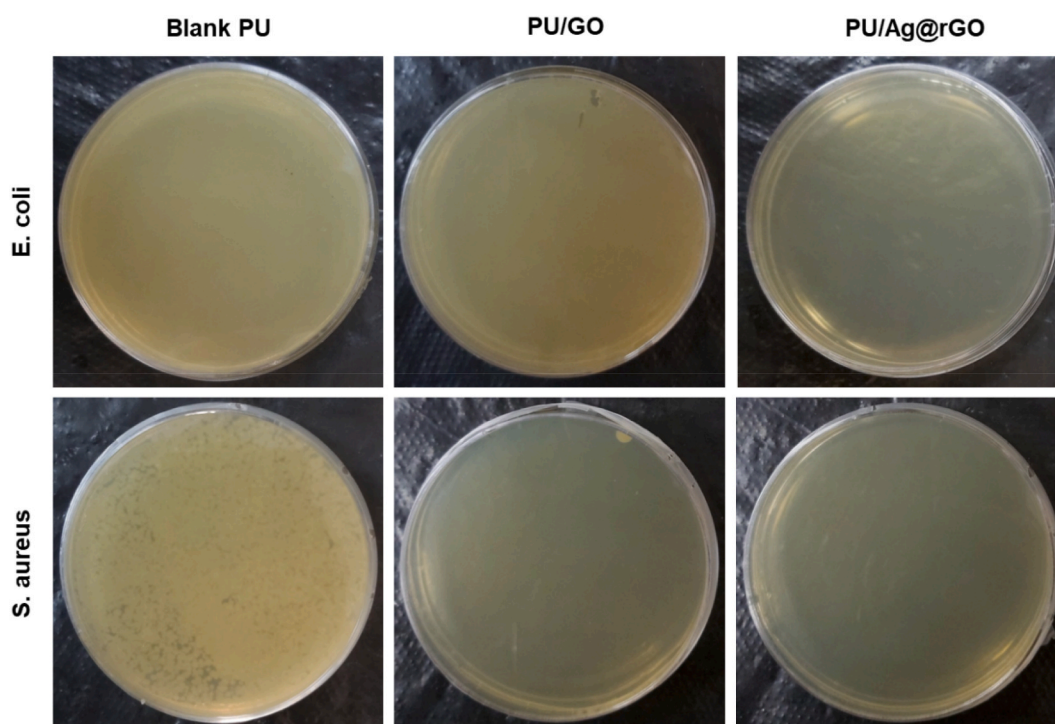**Fig. 7.** SEM images of the prepared PU/GO and PU/Ag@rGO films.

Fig. 8. Evaluation of the antibacterial activity of the prepared films through the bacterial colonies formed after 24 h of incubation.

than for the Blank PU (29.8 %) and PU/GO (59.1 %) samples. The high efficiency of the PU nanocomposite samples compared to the Blank PU can be attributed to the incorporation of GO, rGO, and AgNPs nanostructures, which have a significant positive impact on stimulating cell proliferation and migration [68,69].

3.2.7. In vivo wound healing assay

An in vivo assessment of wound healing was conducted on a rat model 7 and 12 days after treatment with the prepared samples (Fig. 10). The treatment of wounds with PU/Ag@rGO demonstrated the best healing efficiency on day 12 due to the stimulating and accelerating effects of rGO and AgNPs on regenerating skin. Additionally, H&E-stained histological images (Fig. 10B) showed that wounds treated with the PU/Ag@rGO nanocomposite had a quicker epithelial regeneration rate with numerous hair follicles compared to the other films. This is due to the synergistic effects of rGO and Ag nanostructures with desired bioavailability, which provide an
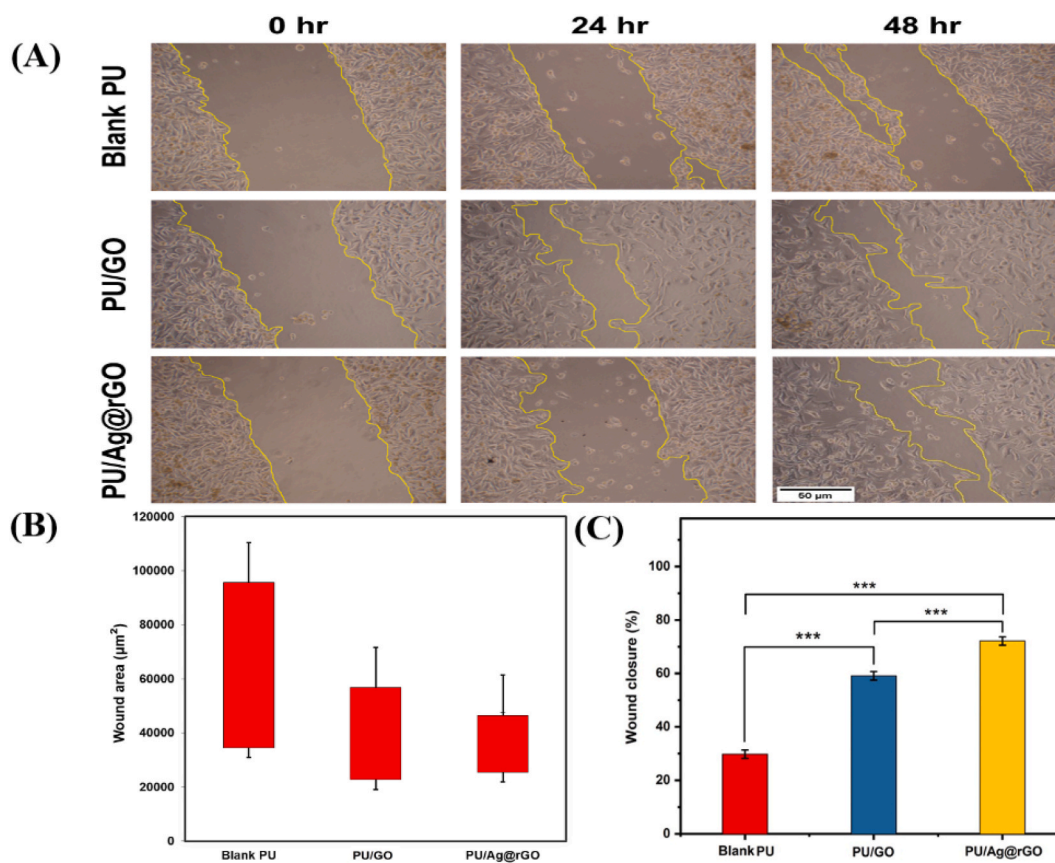
Fig. 9. In vitro scratch wound assay: the optical images of L929 fibroblast cell migration on the films after 24 and 48 h of scratch (A), The remained wound area at three different time point: 0, 24 and 48 h. (B), The wound closure percentage of the scratched area after 48 h (***P < 0.001) (C).

antibacterial environment that effectively encourages granulation tissue, such as fibroblasts proliferation and neovascularization [68, 69].

4. Conclusion

In this study, a highly efficient castor oil-based polyurethane/Ag@rGO nanocomposite was prepared as a promising antibacterial wound dressing. The nanocomposite films were synthesized by impregnating Ag@rGO nanostructures, prepared using microwave assistance, into the castor oil-based PU matrix. SEM analysis showed a high bioavailability of AgNPs and good dispersibility of Ag@rGO nanostructures in the PU/Ag@rGO sample compared to the PU/GO sample. Furthermore, XRD and DMTA analysis confirmed that the PU/Ag@rGO nanocomposites had lower crystallinity, storage modulus, and Tg compared to Blank PU. This was attributed to the interruption of nanostructures in the hydrogen bonding formation of the hard segments. Among the samples, PU/Ag@rGO exhibited the best antibacterial activity against *E. coli* and *S. aureus* bacteria. The wound scratch assay demonstrated that PU/Ag@rGO significantly increased the viability of L929 fibroblast cells. Moreover, the in vivo treatment of wounds with PU/Ag@rGO was much faster and more efficient than with the other samples and the control. In conclusion, the obtained results indicated that the PU/Ag@rGO film is a suitable wound dressing with excellent antibacterial properties.

Additional information

No additional information is available for this paper.

CRediT authorship contribution statement

Abbas Mohammadi: Writing – review & editing, Writing – original draft, Visualization, Validation, Supervision, Software, Resources, Project administration, Methodology, Investigation, Funding acquisition, Formal analysis, Data curation, Conceptualization. **Zahra Ghorbanian Kerdabadi:** Writing – original draft, Visualization, Validation, Investigation, Formal analysis, Data curation. **Seyed Ahmad Ayati Najafabadi:** Writing – original draft, Visualization, Validation, Software, Methodology. **Alireza Pourali:**
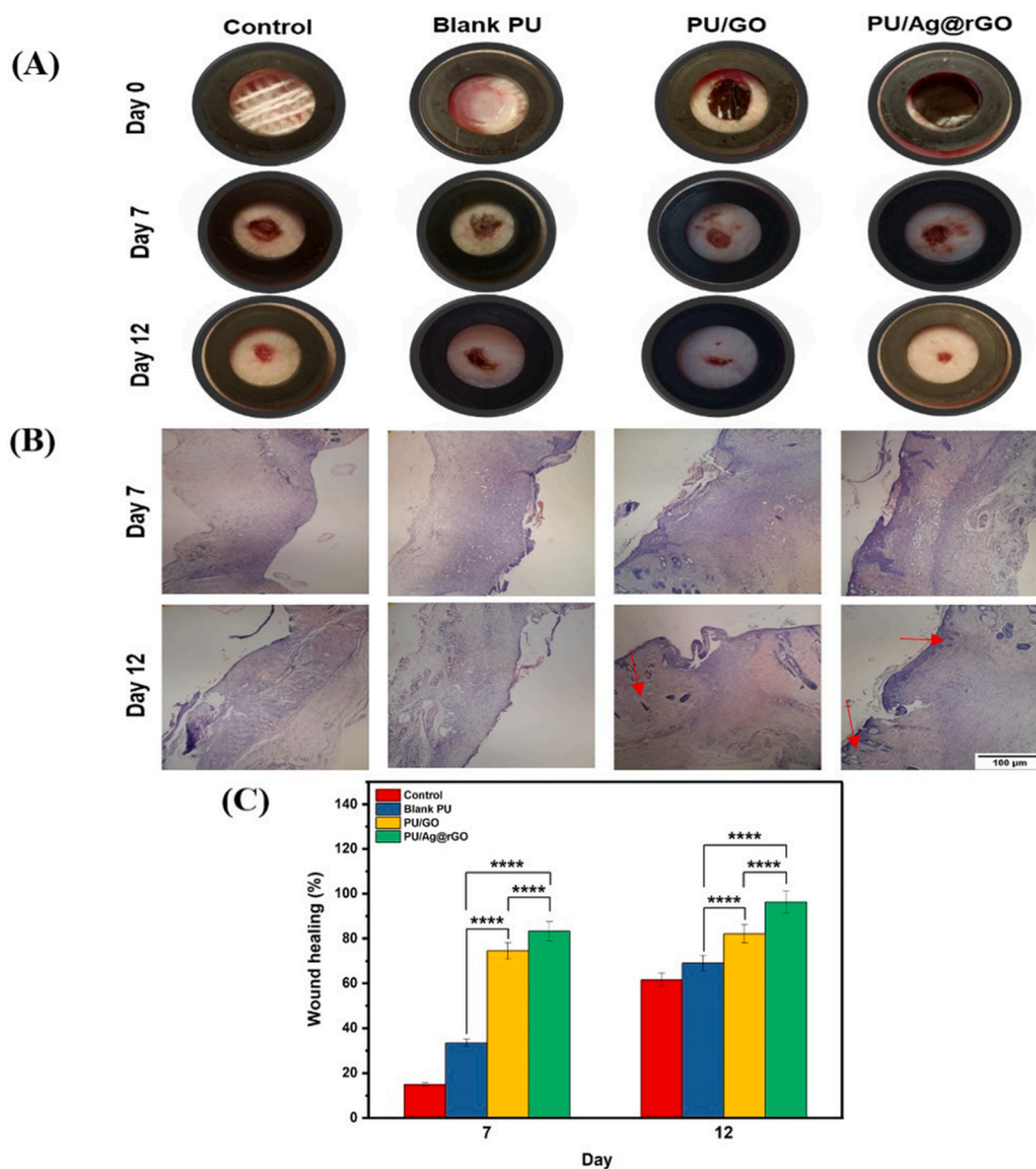
Fig. 10. Photographs taken of the wounds treated with the control, Blank PU, PU/GO and PU/Ag@rGO nanocomposite films at three time points (A); Histologic observation at days 7 and 12 post-surgery: representative images of H&E-stained sections of the subcutaneous tissue surrounding films (B); the percentages of wound healing. Columns were marked with an asterisk (****$P < 0.0001$).

Supervision, Project administration, Funding acquisition. **Fereshteh Nejaddehbashi:** Visualization, Investigation, Formal analysis. **Nastaran Azarbarz:** Visualization, Investigation, Formal analysis. **Kaveh Hatami Kahkesh:** Formal analysis. **Mehrnoosh Ebrahimibagha:** Formal analysis.

Declaration of competing interest

The authors declare that they have no known competing financial interests or personal relationships that could have appeared to influence the work reported in this paper.

Acknowledgements

(Pisa, Italy) for the electron microscopy characterization.

References

[1] J. Ho, et al., Current advancements and strategies in tissue engineering for wound healing: a comprehensive review, Adv. Wound Care 6 (6) (2017) 191–209, https://doi.org/10.1089/wound.2016.0723.

[2] E. Esmaeili, et al., The biomedical potential of cellulose acetate/polyurethane nanofibrous mats containing reduced graphene oxide/silver nanocomposites and curcumin: antimicrobial performance and cutaneous wound healing, Int. J. Biol. Macromol. 152 (2020) 418–427, https://doi.org/10.1016/j.ijbiomac.2020.02.295.

[3] S.A.A. Najafabadi, A. Mohammadi, A.Z. Kharazi, Polyurethane nanocomposite impregnated with chitosan-modified graphene oxide as a potential antibacterial wound dressing, Mater. Sci. Eng. C 115 (2020), 110899, https://doi.org/10.1016/j.msec.2020.110899.

[4] M. Alavi, R.S. Varma, Antibacterial and wound healing activities of silver nanoparticles embedded in cellulose compared to other polysaccharides and protein polymers, Cellulose 28 (13) (2021) 8295–8311, https://doi.org/10.1007/s10570-021-04067-3.

[5] A.J. Hassiba, et al., Review of recent research on biomedical applications of electrospun polymer nanofibers for improved wound healing, Nanomedicine 11 (6) (2016) 715–737, https://doi.org/10.2217/nnm.15.211.

[6] M. Talikowska, X. Fu, G. Lisak, Application of conducting polymers to wound care and skin tissue engineering: a review, Biosens. Bioelectron. 135 (2019) 50–63, https://doi.org/10.1016/j.bios.2019.04.001.

[7] Z. Jian, et al., Polyurethane-modified graphene oxide composite bilayer wound dressing with long-lasting antibacterial effect, Mater. Sci. Eng. C 111 (2020), 110833, https://doi.org/10.1016/j.msec.2020.110833.

[8] M.A. Teixeira, et al., Electrospun nanocomposites containing cellulose and its derivatives modified with specialized biomolecules for an enhanced wound healing, Nanomaterials 10 (3) (2020) 557, https://doi.org/10.3390/nano10030557.

[9] A. Mohammadi, et al., Improvement in bioavailability of curcumin within the castor-oil based polyurethane nanocomposite through its conjugation on the surface of graphene oxide nanosheets, Polym. Adv. Technol. 33 (4) (2022) 1126–1136, https://doi.org/10.1002/pat.5586.

[10] A. Dias, et al., Development of natural-based wound dressings impregnated with bioactive compounds and using supercritical carbon dioxide, Int. J. Pharm. 408 (1–2) (2011) 9–19, https://doi.org/10.1016/j.ijpharm.2011.01.063.

[11] A. Rahmani Del Bakhshayesh, et al., Recent advances on biomedical applications of scaffolds in wound healing and dermal tissue engineering, Artif. Cell Nanomed. Biotechnol. 46 (4) (2018) 691–705, https://doi.org/10.1080/21691401.2017.1349778.

[12] W. Wang, C. Wang, *Polyurethane for Biomedical Applications: A Review of Recent Developments*. The Design and Manufacture of Medical Devices, 2012, pp. 115–151, https://doi.org/10.1533/9781908818188.115.

[13] J.-T. Sun, et al., Polyurethane/nanosilver-doped halloysite nanocomposites: thermal, mechanical properties, and antibacterial properties, Polymers 12 (11) (2020) 2729, https://doi.org/10.3390/polym12112729.

[14] A. Mohammadi, M. Barikani, M. Barmar, Effect of polyol structure on the properties of the resultant magnetic polyurethane elastomer nanocomposites, Polym. Adv. Technol. 24 (11) (2013) 978–985, https://doi.org/10.1002/pat.3173.

[15] C. Zhang, et al., Recent advances in vegetable oil-based polymers and their composites, Prog. Polym. Sci. 71 (2017) 91–143, https://doi.org/10.1016/j.progpolymsci.2016.12.009.

[16] A. Mohammadi, et al., Antibacterial Host–guest intercalated LDH-adorned polyurethane for accelerated dermal wound healing, ACS Appl. Bio Mater. 5 (12) (2022) 5800–5815, https://doi.org/10.1021/acsabm.2c00805.

[17] D.P. Pfister, Y. Xia, R.C. Larock, Recent advances in vegetable oil-based polyurethanes, ChemSusChem 4 (6) (2011) 703–717, https://doi.org/10.1002/cssc.201000378.

[18] A.M. Díez-Pascual, A.L. Díez-Vicente, Wound healing bionanocomposites based on castor oil polymeric films reinforced with chitosan-modified ZnO nanoparticles, Biomacromolecules 16 (9) (2015) 2631–2644, https://doi.org/10.1021/acs.biomac.5b00447.

[19] C.-H. Tsou, et al., Synthesis and properties of antibacterial polyurethane with novel Bis (3-pyridinemethanol) silver chain extender, Polymer 85 (2016) 96–105, https://doi.org/10.1016/j.polymer.2016.01.042.

[20] K.M. Rao, et al., One-pot synthesis of ZnO nanobelt-like structures in hyaluronan hydrogels for wound dressing applications, Carbohydr. Polym. 223 (2019), 115124, https://doi.org/10.1016/j.carbpol.2019.115124.

[21] X. Zhong, et al., Titanium dioxide/quaternary phosphonium salts/polyacrylonitrile composite nanofibrous membranes with high antibacterial properties and ultraviolet resistance efficiency, J. Mater. Sci. 54 (20) (2019) 13322–13333, https://doi.org/10.1007/s10853-019-03833-w.

[22] E. Shams, et al., Polyurethane/siloxane membranes containing graphene oxide nanoplatelets as antimicrobial wound dressings: in vitro and in vivo evaluations, J. Mater. Sci. Mater. Med. 28 (5) (2017) 1–14, https://doi.org/10.1007/s10856-017-5881-z.

[23] Q.H. Tran, A.-T. Le, Silver nanoparticles: synthesis, properties, toxicology, applications and perspectives, Adv. Nat. Sci. Nanosci. Nanotechnol. 4 (3) (2013), 033001, https://doi.org/10.1088/2043-6262/4/3/033001.

[24] J.C. Tiller, Antimicrobial Surfaces, Bioactive surfaces, 2010, pp. 193–217, https://doi.org/10.1007/12_2010_101.

[25] M. Cobos, et al., Graphene oxide–silver nanoparticle nanohybrids: synthesis, characterization, and antimicrobial properties, Nanomaterials 10 (2) (2020) 376, https://doi.org/10.3390/nano10020376.

[26] E.-R. Kenawy, S. Worley, R. Broughton, The chemistry and applications of antimicrobial polymers: a state-of-the-art review, Biomacromolecules 8 (5) (2007) 1359–1384, https://doi.org/10.1021/bm061150q.

[27] H. Bakhshi, et al., Synthesis and characterization of antibacterial polyurethane coatings from quaternary ammonium salts functionalized soybean oil based polyols, Mater. Sci. Eng. C 33 (1) (2013) 153–164, https://doi.org/10.1016/j.msec.2012.08.023.

[28] C.A. Dos Santos, et al., Silver nanoparticles: therapeutical uses, toxicity, and safety issues, J. Pharmaceut. Sci. 103 (7) (2014) 1931–1944, https://doi.org/10.1002/jps.24001.

[29] D. Macocinschi, et al., Thermal and hydrolytic stability of silver nanoparticle polyurethane biocomposites for medical applications, Polym. Degrad. Stabil. 121 (2015) 238–246, https://doi.org/10.1016/j.polymdegradstab.2015.09.017.

[30] M. Alavi, N. Karimi, Biosynthesis of Ag and Cu NPs by secondary metabolites of usnic acid and thymol with biological macromolecules aggregation and antibacterial activities against multi drug resistant (MDR) bacteria, Int. J. Biol. Macromol. 128 (2019) 893–901, https://doi.org/10.1016/j.ijbiomac.2019.01.177.

[31] M. Alavi, N. Karimi, Hemoglobin self-assembly and antibacterial activities of bio-modified Ag-MgO nanocomposites by different concentrations of Artemisia haussknechtii and Protoparmeliopsis muralis extracts, Int. J. Biol. Macromol. 152 (2020) 1174–1185, https://doi.org/10.1016/j.ijbiomac.2019.10.207.

[32] P. Singh, et al., Silver nanoparticles produced from Cedecea sp. exhibit antibiofilm activity and remarkable stability, Sci. Rep. 11 (1) (2021) 1–13, https://doi.org/10.1038/s41598-021-92006-4.

[33] G.A. Sotiriou, S.E. Pratsinis, Antibacterial activity of nanosilver ions and particles, Environ. Sci. Technol. 44 (14) (2010) 5649–5654, https://doi.org/10.1021/es101072s.

[34] M. Taran, M. Rad, M. Alavi, Characterization of Ag nanoparticles biosynthesized by Bacillus sp. HAI4 in different conditions and their antibacterial effects, J. Appl. Pharmaceut. Sci. 6 (11) (2016) 94–99, https://doi.org/10.7324/JAPS.2016.601115.

[35] J. Hussein, et al., Solvent-free and one-pot synthesis of silver and zinc oxide nanoparticles: activity toward cell membrane component and insulin signaling pathway in experimental diabetes, Colloids Surf. B Biointerfaces 170 (2018) 76–84, https://doi.org/10.1016/j.colsurfb.2018.05.058.

[36] M. Alavi, R.S. Varma, Phytosynthesis and modification of metal and metal oxide nanoparticles/nanocomposites for antibacterial and anticancer activities: recent advances, Sustainable Chemistry and Pharmacy 21 (2021), 100412, https://doi.org/10.1016/j.scp.2021.100412.

[37] S.M. Gamboa, et al., Synthesis and characterization of silver nanoparticles and their application as an antibacterial agent, Int. J. Biosen. Bioelectron 5 (2019) 166–173, https://doi.org/10.15406/ijbsbe.2019.05.00172.

[38] C. Li, et al., The antifungal activity of graphene oxide–silver nanocomposites, Biomaterials 34 (15) (2013) 3882–3890, https://doi.org/10.1016/j.biomaterials.2013.02.001.

[39] Z. Zhong, et al., High-performance anionic waterborne polyurethane/Ag nanocomposites with excellent antibacterial property via in situ synthesis of Ag nanoparticles, RSC Adv. 7 (67) (2017) 42296–42304, https://doi.org/10.1039/C7RA08464A.

[40] R. Qu, et al., Preparation and property of polyurethane/nanosilver complex fibers, Appl. Surf. Sci. 294 (2014) 81–88, https://doi.org/10.1016/j.apsusc.2013.11.116.

[41] H.V. Tran, et al., Synthesis, characterization, antibacterial and antiproliferative activities of monodisperse chitosan-based silver nanoparticles, Colloids Surf. A Physicochem. Eng. Asp. 360 (1–3) (2010) 32–40, https://doi.org/10.1016/j.colsurfa.2010.02.007.

[42] S.W. Chook, et al., Antibacterial performance of Ag nanoparticles and AgGO nanocomposites prepared via rapid microwave-assisted synthesis method, Nanoscale Res. Lett. 7 (1) (2012) 1–7, https://doi.org/10.1186/1556-276X-7-541.

[43] T. Long, et al., Facile synthesis of Ag-reduced graphene oxide hybrids and their application in electromagnetic interference shielding, Appl. Phys. A 116 (1) (2014) 25–32, https://doi.org/10.1007/s00339-014-8517-x.

[44] Z. Zhang, et al., Sodium citrate: a universal reducing agent for reduction/decoration of graphene oxide with au nanoparticles, Nano Res. 4 (2011) 599–611, https://doi.org/10.1007/s12274-011-0116-y.

[45] S. Yu, et al., Transformation kinetics of silver nanoparticles and silver ions in aquatic environments revealed by double stable isotope labeling, Environ. Sci.: Nano 3 (4) (2016) 883–893, https://doi.org/10.1039/C6EN00104A.

[46] K. Seku, et al., Microwave-assisted synthesis of silver nanoparticles and their application in catalytic, antibacterial and antioxidant activities, Journal of Nanostructure in Chemistry 8 (2018) 179–188, https://doi.org/10.1007/s40097-018-0264-7.

[47] H. Barani, B. Mahltig, Microwave-assisted synthesis of silver nanoparticles: effect of reaction temperature and precursor concentration on fluorescent property, J. Cluster Sci. (2020) 1–11, https://doi.org/10.1007/s10876-020-01945-x.

[48] X. Zhao, et al., Microwave-assisted synthesis of silver nanoparticles using sodium alginate and their antibacterial activity, Colloids Surf. A Physicochem. Eng. Asp. 444 (2014) 180–188, https://doi.org/10.1016/j.colsurfa.2013.12.008.

[49] Y.A. Rodríguez Nuñez, et al., Preparation of hydrogel/silver nanohybrids mediated by tunable-size silver nanoparticles for potential antibacterial applications, Polymers 11 (4) (2019) 716, https://doi.org/10.3390/polym11040716.

[50] R. Zhao, et al., Stable nanocomposite based on PEGylated and silver nanoparticles loaded graphene oxide for long-term antibacterial activity, ACS Appl. Mater. Interfaces 9 (18) (2017) 15328–15341, https://doi.org/10.1021/acsami.7b03987.

[51] L. Li, et al., Preparation of magnetic ionic liquid/chitosan/graphene oxide composite and application for water treatment, Int. J. Biol. Macromol. 66 (2014) 172–178, https://doi.org/10.1016/j.ijbiomac.2014.02.031.

[52] Y. Li, et al., Microwave-assisted synthesis of Ag/rGO composites and their cytotoxicity for HT22 Neuronal cell, Mater. Res. Innovat. 21 (4) (2017) 257–261, https://doi.org/10.1080/14328917.2016.1212511.

[53] B. Fan, et al., Facile one-pot preparation of silver/reduced graphene oxide nanocomposite for cancer photodynamic and photothermal therapy, J. Nanosci. Nanotechnol. 16 (7) (2016) 7049–7054, https://doi.org/10.1166/jnn.2016.11327.

[54] A.T. Habte, D.W. Ayele, Synthesis and characterization of reduced graphene oxide (rGO) started from graphene oxide (GO) using the tour method with different parameters, Adv. Mater. Sci. Eng. (2019), https://doi.org/10.1155/2019/5058163, 2019.

[55] P.A. Bozkurt, Sonochemical green synthesis of Ag/graphene nanocomposite, Ultrason. Sonochem. 35 (2017) 397–404, https://doi.org/10.1016/j.ultsonch.2016.10.018.

[56] S.N. Alam, N. Sharma, L. Kumar, Synthesis of graphene oxide (GO) by modified hummers method and its thermal reduction to obtain reduced graphene oxide (rGO), Graphene 6 (1) (2017) 1–18, https://doi.org/10.4236/graphene.2017.61001.

[57] N. Sharma, et al., Synthesis and characterization of graphene oxide (GO) and reduced graphene oxide (rGO) for gas sensing application, in: Macromolecular Symposia, Wiley Online Library, 2017, https://doi.org/10.1002/masy.201700006.

[58] G. Xu, et al., Preparation, photoluminescence properties and application for in vivo tumor imaging of curcumin derivative-functionalized graphene oxide composite, Dyes Pigments 141 (2017) 470–478, https://doi.org/10.1016/j.dyepig.2017.02.046.

[59] S. Vinay, et al., Hydrothermal synthesis of Ag/rGO@ CTFE nanocomposite as a promising photocatalyst for degradation action, J. Mol. Struct. 1228 (2021), 129722, https://doi.org/10.1016/j.molstruc.2020.129722.

[60] M. Moghayedi, et al., Kinetics and mechanism of antibacterial activity and cytotoxicity of Ag-RGO nanocomposite, Colloids Surf. B Biointerfaces 159 (2017) 366–374, https://doi.org/10.1016/j.colsurfb.2017.08.001.

[61] P. Pokharel, D.S. Lee, Thermal and mechanical properties of reduced graphene oxide/polyurethane nanocomposite, J. Nanosci. Nanotechnol. 14 (8) (2014) 5718–5721, https://doi.org/10.1166/jnn.2014.8824.

[62] M. Panahi-Sarmad, et al., Programing polyurethane with systematic presence of graphene-oxide (GO) and reduced graphene-oxide (rGO) platelets for adjusting of heat-actuated shape memory properties, Eur. Polym. J. 118 (2019) 619–632, https://doi.org/10.1016/j.eurpolymj.2019.06.034.

[63] Y. Ahmadi, M. Yadav, S. Ahmad, Oleo-polyurethane-carbon nanocomposites: effects of in-situ polymerization and sustainable precursor on structure, mechanical, thermal, and antimicrobial surface-activity, Compos. B Eng. 164 (2019) 683–692, https://doi.org/10.1016/j.compositesb.2019.01.078.

[64] A. Mohammadi, et al., Silver (I) complex with a Schiff base ligand extended waterborne polyurethane: a developed strategy to obtain a highly stable antibacterial dispersion impregnated with in situ formed silver nanoparticles, Chem. Eng. J. 381 (2020), 122776, https://doi.org/10.1016/j.cej.2019.122776.

[65] J.W. Cho, J.H. So, Polyurethane–silver fibers prepared by infiltration and reduction of silver nitrate, Mater. Lett. 60 (21–22) (2006) 2653–2656, https://doi.org/10.1016/j.matlet.2006.01.072.

[66] S. Yang, et al., Controllable Ag-rGO heterostructure for highly thermal conductivity in layer-by-layer nanocellulose hybrid films, Chem. Eng. J. 383 (2020), 123072, https://doi.org/10.1016/j.cej.2019.123072.

[67] V. Palmieri, et al., The future development of bacteria fighting medical devices: the role of graphene oxide, Expet Rev. Med. Dev. 13 (11) (2016) 1013–1019, https://doi.org/10.1080/17434440.2016.1245612.

[68] J. Franková, et al., Effects of silver nanoparticles on primary cell cultures of fibroblasts and keratinocytes in a wound-healing model, J. Appl. Biomater. Funct. Mater. 14 (2) (2016) 137–142, https://doi.org/10.5301/jabfm.5000268.

[69] Z. Sadat, et al., A comprehensive review on the applications of carbon-based nanostructures in wound healing: from antibacterial aspects to cell growth stimulation, Biomater. Sci. 10 (24) (2022) 6911–6938, https://doi.org/10.1039/D2BM01308H.